SCIENTIFIC REPORTS

OPEN

SUBJECT AREAS:
ELECTRONIC AND SPINTRONIC DEVICES
ELECTRICAL AND ELECTRONIC ENGINEERING
ELECTRONIC PROPERTIES AND DEVICES

Received
14 November 2013

Accepted
17 January 2014

Published
5 February 2014

Correspondence and requests for materials should be addressed to F.A.-D. (ferasa@student.unimelb.edu.au)

All-Graphene Planar Self-Switching MISFEDs, Metal-Insulator-Semiconductor Field-Effect Diodes

Feras Al-Dirini[1,2,3], Faruque M. Hossain[1,2,3], Ampalavanapillai Nirmalathas[1,2] & Efstratios Skafidas[1,2,3]

[1]Department of Electrical and Electronic Engineering, University of Melbourne, VIC 3010, Australia, [2]Optics and Nanoelectronics Research Group, National ICT Australia, VIC 3010, Australia, [3]Centre for Neural Engineering, University of Melbourne, VIC 3010, Australia.

Graphene normally behaves as a semimetal because it lacks a bandgap, but when it is patterned into nanoribbons a bandgap can be introduced. By varying the width of these nanoribbons this band gap can be tuned from semiconducting to metallic. This property allows metallic and semiconducting regions within a single Graphene monolayer, which can be used in realising two-dimensional (2D) planar Metal-Insulator-Semiconductor field effect devices. Based on this concept, we present a new class of nano-scale planar devices named Graphene Self-Switching MISFEDs (Metal-Insulator-Semiconductor Field-Effect Diodes), in which Graphene is used as the metal and the semiconductor concurrently. The presented devices exhibit excellent current-voltage characteristics while occupying an ultra-small area with sub-10 nm dimensions and an ultimate thinness of a single atom. Quantum mechanical simulation results, based on the Extended Huckel method and Nonequilibrium Green's Function Formalism, show that a Graphene Self-Switching MISFED with a channel as short as 5 nm can achieve forward-to-reverse current rectification ratios exceeding 5000.

Graphene, an atomically-thin sheet of carbon atoms[1], has opened many opportunities in the field of electronics due to its unique electronic properties[2,3] including enhanced performance electronics and sensors[4]. The realization of high frequency Graphene FETs[5–8] has led to the realization of wafer scale Graphene integrated circuits[9] with FETs that have enhanced functionalities[10,11]. More recently, new classes of devices have been realized by exploiting some of Graphene's unique properties[12,13]. On the other hand, realization of Graphene-based diodes has received much less attention. High performance diodes will enable next generation terahertz detectors and new RF systems, but their realization at the nano-scale with high operation frequency has been a challenge. Graphene-based schottky diodes, in which Graphene was used as the metal[14–16] or the semiconductor[17], have been realized, but are limited to large sizes for high frequency operation. The nano-scale alternative to a schottky diode would be a diode-connected FET, but this extra diode connection introduces increased parasitic capacitances and inductances that limit the operation frequency of the diode-connected FET.

In order to overcome this problem diodes based on new rectification mechanisms were proposed, one of which was the Self-Switching Diode (SSD)[18]. A SSD is an asymmetrical nanowire in which rectification occurs due to a self-induced field-effect that enhances conduction through the nanowire in one direction, while suppressing it in the opposite direction. Self-Switching Diodes showed excellent high frequency performance at 110 GHz[19], and were later demonstrated as room-temperature Terahertz detectors[20]. Self-switching diodes are two-dimensional (2D) planar devices that require very minimal lithography steps during fabrication and are very well suited for a two dimensional material like Graphene. Nevertheless, these devices suffer from the constraint of not having a metallic gate, as the channel (the nanowire) and the side gates in them need to be made from the same material, which is usually a semiconductor. Until recently there was no single material that could have metallic regions and also semiconducting regions within the same plane, until the discovery of Graphene Nanoribbons (GNRs)[21,22].

Graphene Nanoribbons, which are long narrow strips of Graphene, can be either zigzag-edged or armchair-edged and can behave as metallic or semiconducting respectively[23]. Etching GNRs with smooth edges[24–30] or realizing them through other means[31–34] has been making good progress in recent years, and this can lead to the ability of making zGNRs and aGNRs from a single Graphene monolayer. This would mean that, within a single Graphene monolayer, metallic and semiconducting regions can be formed, and a number of planar atomically-thin 2D devices have been proposed based on this concept[35,36]. Moreover, these devices may also be intercon-

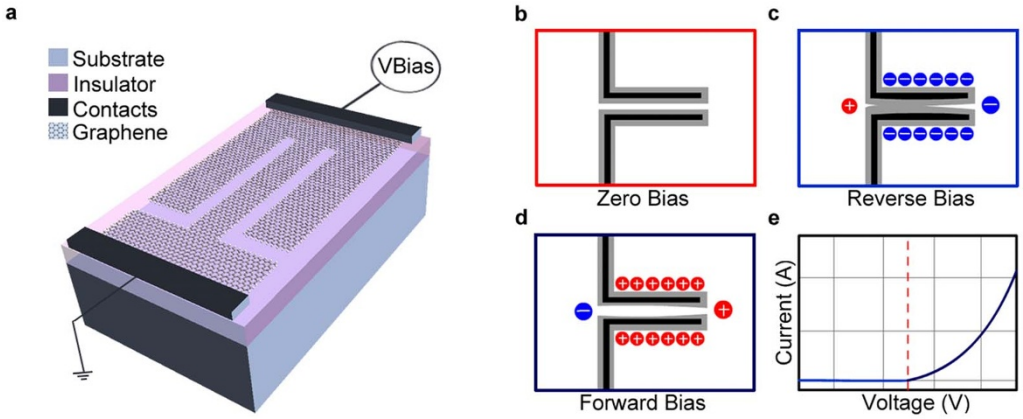

Figure 1 | Graphene Self-Switching Diode (G-SSD) architecture and principle of operation. (a), schematic diagram showing the structure and architecture of a G-SSD and showing the biasing direction of the device. (b), illustration showing where the natural depletion regions (grey regions) form in a G-SSD due to the presence of surface states at the boundaries of the L-shaped trenches. (c), illustration showing how the depletions regions are widened eventually pinching-off the channel due to the application of a negative bias voltage across the device. (d), illustration showing how the depletion regions are narrowed eventually opening up the channel due to the application of a positive bias voltage across the device. (e), expected I-V characteristics of the device. The light blue part of the curve represents the region in which the device has a pinched-off channel and is not conducting, while the dark blue part of the curve represents the region in which the device has an open channel and is conducting.

nected within the same single Graphene monolayer using GNRs[37], which may lead to not only atomically-thin devices, but more interestingly, all-Graphene atomically-thin electronic circuits. However, it is important to note that there is a great limitation in this, as these regions can only be realized at an angle to each other, since the different edge shapes arise from etching at different angles[38]. This would exclude all types of field effect devices, since the field in them is usually applied from a metallic region that is directly adjacent to a semiconducting region.

Here we show how etching a Graphene monolayer into adjacent parallel aGNRs with precisely defined edges, can give rise to high performance nano-scale field effect devices that are planar and completely 2D, i.e. atomically thin. Armchair GNRs are generally semiconducting and exhibit a bandgap, but at certain widths they start to behave as metals with vanishingly small band gaps or no band gaps at all[39]. This occurs in aGNRs that have a width of $3p + 2$ carbon atoms, where p is an integer. For all other widths, aGNRs are semiconducting.

By exploiting this property we propose a new class of self-switching diodes that have metallic gates controlling a semiconducting channel, all built with a single Graphene monolayer, and we refer to these devices here as a Graphene Self-Switching MISFEDs (Metal-Insulator-Semiconductor Field-Effect Diodes). Both the metal and the semiconductor in these devices are aGNRs but with different widths, separated by an insulating region. The devices we propose are at sub-10 nm dimensions and still achieve forward-to-reverse current rectification ratios exceeding 5000.

We begin by highlighting how the constraint of not having a metallic gate in a SSD limits its performance, and then we show how a Graphene SSD (G-SSD) can be transformed into a much more superior Graphene Self-Switching MISFED (G-SS MISFED) by tackling this issue, highlighting this through the comparison of the performance of both devices.

Results

The Graphene Self-Switching Diode (G-SSD). Self-Switching Diodes are formed by etching two L-shaped trenches back-to-back forming a narrow nano-channel in between them, through which conduction occurs. The conductance of this nano-channel is controlled by a field effect, which is applied by two side gates surrounding the channel, and these are connected to one of the two-terminals of the device. The geometry of the device (Fig. 1(a)) and its principle of operation are illustrated in Fig. 1. With no bias voltage applied, natural depletion regions are formed at the edges of the nano-channel due to the presence of surface energy states at the edges of the L-shaped trenches (Fig. 1(b)). Applying a negative bias voltage widens these depletion regions eventually pinching-off the channel and suppressing current flow through it in the reverse direction (Fig. 1(c)). On the other hand, a positive applied voltage results in narrowing the depletion regions, eventually opening up the channel and allowing current conduction in the forward direction (Fig. 1(d)). This unidirectional current flow results in non-linear current-voltage characteristics very similar to those of a conventional diode (Fig. 1(e)).

The nano-channel in a G-SSD is a Graphene nano-ribbon, and in order to control the conductance of this channel by an electric field it needs to be semiconducting, this is achieved using an aGNR. A corollary to this is that a G-SSD geometry with a zGNR channel should not behave like a diode if the rectification mechanism in a G-SSD is purely based on an electric field effect, since zGNRs are metallic and a metal's conductance should not be affected by an electric field. In order to confirm this, we use Nonequilibrium Green's Function Formalism and a tight-binding model based on the Extended Huckel (EH) Method[40] as implemented in Quantum Wise Atomistic Tool Kit[40] (calculation details are discussed in the methods section), to calculate the I-V characteristics of two G-SSD device geometries, one with a zGNR channel and the other with an aGNR channel. The simulated device geometries are shown in Figs. 2(a) and 2(c) respectively, while their I-V characteristics are shown in Figs. 2(b) and 2(d) respectively.

Figure 2(b) shows a linear I-V relationship for the G-SSD geometry with a zGNR, representing no rectification and confirming that rectification in a G-SSD is a field effect phenomenon, and is not related to other transport mechanisms. On the other hand Fig. 2(d) does show a clearly non-linear I-V response curve for a G-SSD with an aGNR channel, but asymmetry is not noticeable, and consequently no rectification occurs. In order to understand this, further analysis of the device geometry presented in Fig. 2(c) is required.

As can be seen from Fig. 2(c), having a semiconducting aGNR channel would also require having the side gates as aGNRs. This means that the side gates are also semiconducting, as is the case with any SSD. In Fig. 2(c) the channel is 6 atoms wide, and so are each of the side gates, and since all of them are semiconducting and equal in size it is expected that they will affect each other equally. This means that depletion regions will form, not only in the channel, but also in

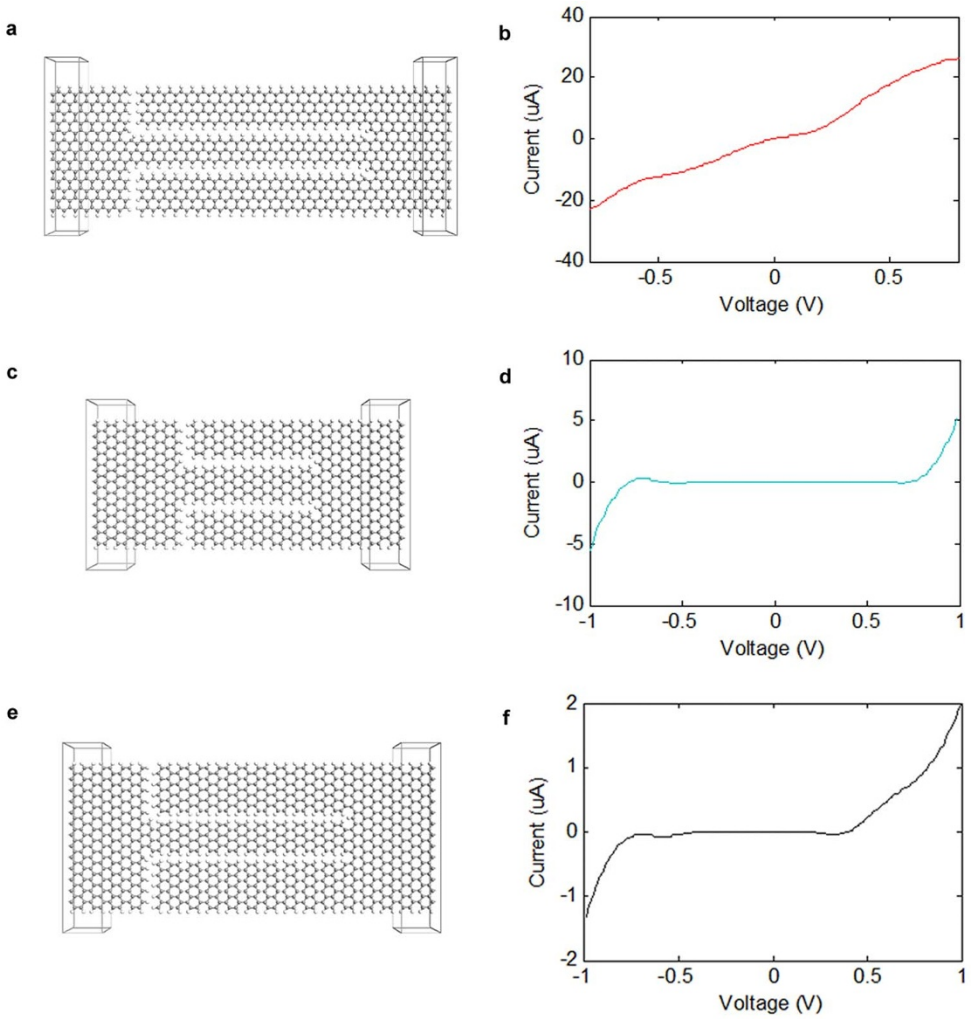

Figure 2 | Comparison between different G-SSD types. (a), a G-SSD structure with a metallic zigzag GNR as the channel. All dangling carbon bonds are passivated with hydrogen in this device and in all subsequent device structures, unless stated otherwise. (b), the simulated I-V characteristics of the device in (a) showing an almost linear response with no rectification and very high current values due to the metallic behaviour of the channel. (c), a G-SSD structure with a semiconducting armchair GNR as the channel. The channel and the two side gates are chosen to be 6 atoms wide making them all equal in width. (d), the I-V characteristics of the device in (c) showing a non-linear response that is almost symmetrical due to the image field-effect from the channel on to the gates and vice versa. (e), a G-SSD sturcuture with a semiconducting armchair GNR as the channel. The channel is chosen to be 6 atoms wide, while the two side gates are chosen to be 9 atoms wide respectively, and the channel is made longer than the channel of the device in (c). (f), the I-V characterisitics of the device in (e) showing a non-linear response with significant asymmetry achieving proper rectification. The threshold turn-on voltage of the device is about 0.4 V, while the reverse breakdown voltage of the device is about −0.75 V. Within the rectification region of operation (−0.75 V–0.75 V) the rectification ratio of the device reaches almost one order of magnitude.

the gates, resulting in what may be referred to as an image field effect from the channel on to the gates. This is illustrated in Fig. 1(b). This image effect greatly weakens the control the gates can have on the channel's conductance, and since in this case the gates are equal in size to the channel, it is expected that they will not be able to control the channel. However, this also implies that if the gates are larger in size than the channel, then the effective field generated by the gates on the channel will dominate and hence may have some control over its conductance.

In order to confirm this, another G-SSD device with an aGNR channel was investigated, but this time the gates were made 9 atoms wide, making each of them one and a half times wider than the channel, and is shown in Fig. 2(e). Moreover, the channel length was made longer, in order to increase the interacting area between the gates and the channel, and achieve better field-effect control. The I-V characteristics of the optimized device are shown in Fig. 2(f), and as expected, they show very good asymmetry; in which forward conduction is enhanced while reverse conduction is suppressed. The optimized device achieves a relatively comparable rectification ratio of forward current to reverse current in comparison with other previously reported SSDs, reaching up to almost one order of magnitude. Nevertheless, this ratio needs to be improved.

Graphene Self-Switching MISFEDs. In order to overcome the limitations of conventional all-semiconducting Self-Switching Diodes, a new class of planar self-switching devices is proposed here, and is named a Graphene Self-Switching MISFED (G-SS MISFED), and is shown in Fig. 3.

Figure 3(a) shows a perspective view of the geometry of a G-SS MISFED, while Figs. 3(b) and 3(c) illustrate the difference between a G-SS MISFED and a G-SSD, respectively. The fundamental difference between the two devices, is that the side gates in a G-SSD are semiconducting, while the side gates in a G-SS MISFED are metallic and the latter is achieved by ensuring that the side gating aGNRs are $3p + 2$ carbon atoms wide. However, it is worth noting that this is only relevant at extremely downscaled dimensions, where quantum

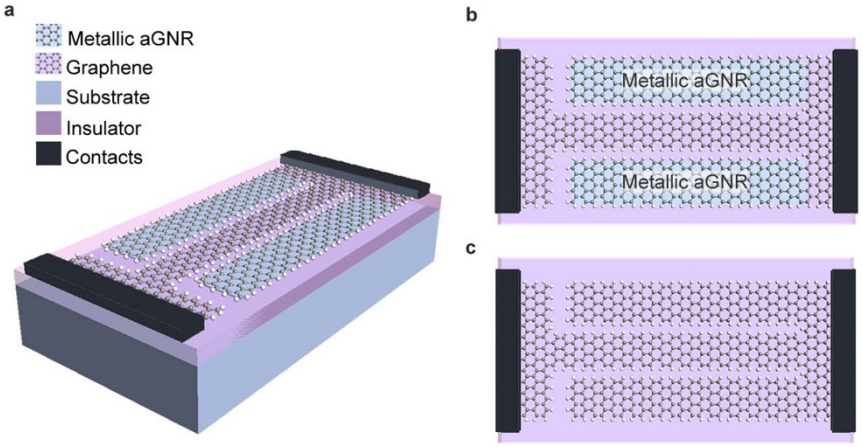

Figure 3 | The fundamental difference between a G-SS MISFED and a G-SSD. (a), a schematic diagram showing a perspective view of the structure of a Graphene Self-Switching MISFED (G-SS MISFED). Graphene regions that are highlighted in blue represent aGNRs that are metallic with a width of $3p + 2$ atoms, where p is an integer. (b), a top-view of the G-SS MISFED in (a) illustrating how the choice of the width of the side gates can make them metallic and highlighting the fundamental difference between a G-SS MISFED and a G-SSD.The side gates are 8 atoms wide. (c), a top-view of a G-SSD showing that the side gates are semiconducting like the channel. The side gates here are 7 atoms wide.

effects dominate, but at larger dimensions, this can also be realized based on a different approach that is experimentally more feasible, without the need for GNRs with perfect edges. This can be achieved through a single etching step, in which the channel is etched down as narrow as possible (narrower than 20 nm), making it semiconducting due to its edge imperfections, while the side gates are defined as wide as possible (at least wider than 50 nm), ensuring that they have very small bandgaps, or no bandgaps at all. Here we will implement the first approach based on the quantum effects in order to investigate the performance of a G-SS MISFED at its ultimate downscaled dimensions.

In order to see how this reflects on the performance of the device, the I-V characteristics of a Graphene Self-Switching MISFED, shown in Fig. 4(a), were calculated using the previously mentioned methods

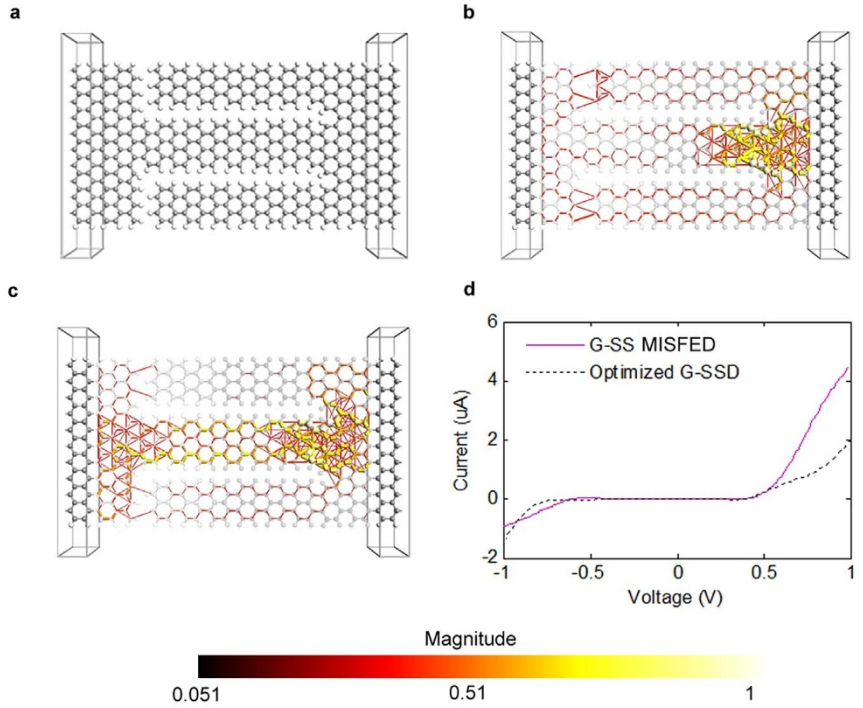

Figure 4 | Transport characteristics of a G-SS MISFED. (a), the structure of the simulated G-SS MISFED. (b), a transmission pathways plot of the device in (a) under reverse bias (−1 V) showing no continuous conduction through the channel and demonstrating how the channel is pinched-off by the field-effect applied through the side gates. Weak but continuous tunneling can be seen across the vertical insulating trenches. This is illustrated by the continuous path of red lines along the edges of the side gates and through the vertical insulating trenches. (c), a transmission pathways plot of the device in (a) under forward bias (1 V) showing continuous conduction through the channel, which is illustrated by the yellow lines along the edges of the channel. The color of a line resembles the magnitude of the local transmission component along a bond according to the color bar at the bottom of the figure. In (b) and (c) the atoms and the bonds in the central region of the device geometry are drawn with 80% transparency to allow better visualization of the transmission pathways. (d), I-V characteristics of the G-SS MISFED in (a) (purple curve) compared with the I-V characteristics of the optimized G-SSD of Fig. 2(e) (dotted black curve), showing the superior performance of the G-SS MISFED.

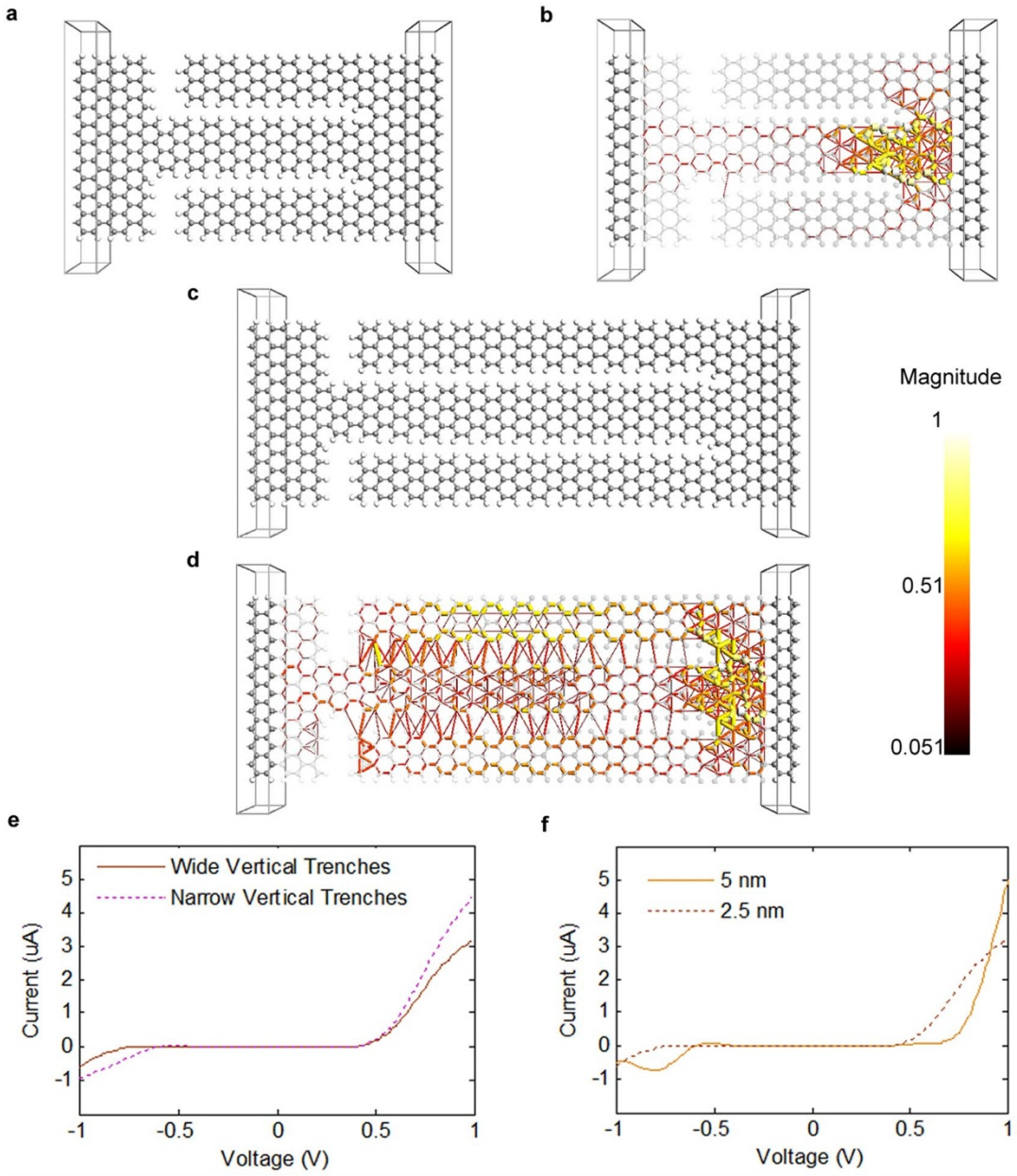

Figure 5 | Optimization of G-SS MISFED geometry. (a), a G-SS MISFED structure similar to the one in Fig. 4(a) but with wider vertical insulating trenches to suppress tunneling current through them. (b), transmission pathways plot for the device in (a) under reverse bias (−1 V), showing suppression of tunneling current through the vertical insulating trenches. (c), a G-SS MISFED structure similar to the one in (a) but with a 5 nm long channel, which is twice as long as the 2.5 nm channel in the device of (a). (d), transmission pathways plot for the device in (c) under reverse bias (−1 V), showing that tunneling current through the horizontal insulating trenches becomes significant when the channel is made twice as long. (e), I-V characteristics of the device in (a) (brown curve) compared with the I-V characteristics of the device of Fig. 4(a) (dotted purple curve). (f), I-V characteristics of the device in (c) (orange curve) compared with the I-V characteristics of the device in (a) (dotted brown curve).

and are shown in Fig. 4 (d). The geometry of the simulated device in Fig. 4(a) represents a comparable geometry to the one in Fig. 2(c), which did not achieve any rectification. The device in Fig. 2(c) had side gating aGNRs that were 6 atoms wide, and hence they were semiconducting, while the device in Fig. 4(a) has side gating aGNRs that are 5 atoms wide, making them metallic. Unlike the I-V characteristics of the G-SSD with similar dimensions shown in Fig. 2(c), the Graphene Self-Switching MISFED shown in Fig. 4(a) shows very good asymmetry and strong rectification. Even when compared with the optimized G-SSD that was presented in Fig. 2(e), the Graphene Self-Switching MISFED without any optimization still greatly outperforms the optimized G-SSD, as shown in Fig. 4(d).

In order to obtain a better understanding of the transport mechanisms in a Graphene Self-Switching MISFED, local current components can be investigated by extracting local transmission mechanisms on an atomic scale. Local charge transmission can be expressed as lines in the direction of the chemical bonds between the atoms, and these lines are referred to as transmission pathways. The thickness and the colour of these lines represent the magnitude of the local charge transmission. Transmission pathways were calculated for the device in Fig. 4(a) under reverse bias (−1 V) and forward bias (+1 V), and are shown as 3D plots in Figs. 4(b) and 4(c) respectively (calculation details are discussed in the methods section).

As expected, under the forward bias case, which is shown in Fig. 4(c), continuous transmission pathways through the channel

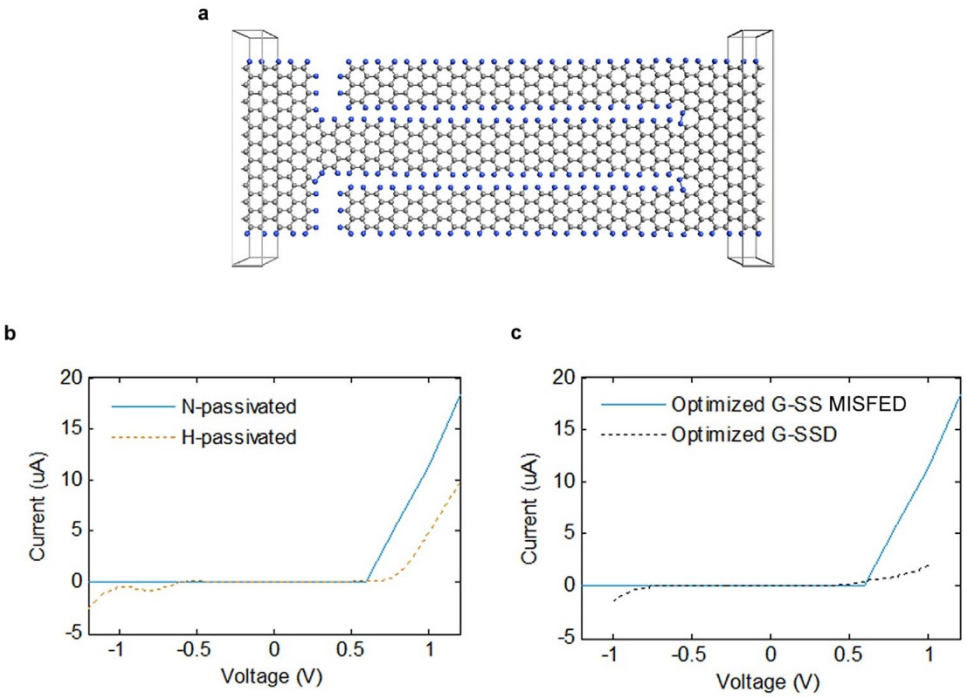

Figure 6 | Nitrogen Passivation. (a), nitrogen passivated G-SS MISFED. The structure of the device is similar to the device in Fig. 5(c) but with nitrogen passivation instead of hydrogen. (b), I-V characteristics of the device in (a) (blue curve) compared with the I-V characteristics of the device of Fig. 5(c) (dotted orange curve), showing a greatly suppressed reverse current and a greatly enhanced forward current. (c), comparrison between the I-V characteristics of the optimized G-SS MISFED in (a) (blue curve) and the optimized G-SSD in Fig. 2(e) (dotted black curve). The forward-to-reverse current rectification ratio of the optimized G-SS MISFED, within the rectification region of operation (−1.2 V–1.2 V) reaches up to 5×10^3, representing an enhancement of almost 3 orders of magnitude when compared with the optimized G-SSD (dotted black curve).

are clearly observed allowing the forward conduction of current through the channel. On the other hand for the reverse bias case it can be clearly observed from Fig. 4(b) that there are no continuous transmission pathways through the channel, and this confirms that the reverse conduction through the channel is greatly suppressed, if not completely blocked. Figure 4(b) confirms the strong effect that the applied field has on controlling the channel's conductance, and illustrates how it leads to the channel's pinch-off, which prevents reverse conduction through it.

However, Fig. 4(b) indicates some continuous transmission pathways through the vertical insulating trenches, suggesting a flow of reverse tunnelling current through these trenches. This tunnelling current explains the flow of reverse current through the device under a reverse bias, as observed in Fig. 4(d).

Optimization of device dimensions. In order to suppress the unwanted tunnelling current through the vertical insulating trenches, these trenches can be made wider, resulting in the structure shown in Fig. 5(a). Figure 5(b) shows the transmission pathways plot of this new geometry under reverse bias (−1 V), and confirms the significant reduction of tunnelling current through the vertical insulating trenches as required. Figure 5(e) shows how this reflects on the I-V characteristics of the device, confirming the suppression of reverse current, but also resulting in weaker forward current. This may be due to the fact that widening the vertical insulating trenches reduces the gated length of the channel and hence weakens the field effect control over its conductance slightly. The length of the channel in the device under investigation is only 2.5 nm, and making it twice as long should not degrade its performance or speed significantly since the transport through the channel is ballistic[41], but could potentially result in stronger control over the channel's conductance.

The channel of the device is made 5 nm long, forming the geometry shown in Fig. 5(c), and its I-V characteristics are shown in Fig. 5(f). From Fig. 5(f) it is clearly seen that forward conduction is significantly enhanced, and this time it was achieved by increasing the length of the gated region of the channel. However, a new phenomenon occurs at reverse bias, as indicated by the non-linear reverse current flow at negative bias voltages. A transmission pathways plot is used once again in order to explore the origins of this non-linear current component, and is shown in Fig. 5(d) for the device under reverse bias (−1 V). Figure 5(d) indicates that this component is due to tunnelling current through the horizontal insulating trenches that isolate the channel from the side gates. It would not be desirable to increase the width of these horizontal trenches, as this would weaken the control that the side gates have over the channel's conductance, and hence a different approach might be needed.

Nitrogen passivation. The problem of tunnelling current that flows from the side gates to the channel through the horizontal insulating trenches may be addressed through better insulation between the side gates and the channel.

Insulation in our Graphene Self-Switching MISFED had been achieved through the etching of L-shaped trenches followed by the passivation of dangling carbon bonds with hydrogen at the edges of the GNRs. It had been proposed earlier that the use of nitrogen for passivation of dangling bonds in GNRs instead of hydrogen, can enhance the performance of GNR field-effect devices such as Graphene Nanopores[42]. This passivation of dangling bonds with nitrogen in GNRs can be achieved by high-power electrical joule heating of the GNRs in ammonia gas[43]. Also interestingly, this process can lead to making GNRs with excess free electron charge carriers[44].

Based on the above, we investigate a new device structure shown in Fig. 6(a), which is similar to the device in Fig. 5(c) but with nitrogen, instead of hydrogen, passivation for dangling carbon bonds at the

edges of the GNRs. The I-V characteristics of this new nitrogen-passivated Graphene Self-Switching MISFED were calculated and are shown in Fig. 6(b). It can be seen from Fig. 6(b) that nitrogen passivation greatly suppresses reverse conduction by preventing the non-linear tunnelling current from flowing through the horizontal insulating trenches, as desired. Interestingly, the effect of the excess free electron charge carriers that nitrogen passivation introduces is clearly apparent through the significant enhancement of forward current through the device. After all the optimization steps presented for the Graphene Self-Switching MISFED, the atomically-thin field-effect diode, which has nano-scale dimensions of only 3 nm × 7 nm and a very short channel length of only 5 nm, was able to achieve a very high forward-to-reverse current rectification ratio of 5000, and this is illustrated in Fig. 6(c).

Discussion

We have presented a new class of planar all-Graphene Metal-Insulator-Semiconductor field-effect devices that are atomically-thin, using a single Graphene monolayer. A new type of device, termed a Graphene Self-Switching MISFED (G-SS MISFED), which is a 2D field-effect diode that incorporates metallic gates used to control a semiconducting channel's conductance by means of a self-induced field-effect, is presented. Both the metallic and the semiconducting regions were constructed from a single Graphene monolayer by patterning it into parallel adjacent aGNRs with varying widths. Insulation between the gates and the channel was achieved by nitrogen passivation. Nitrogen passivation resulted in a material with excess free electron charge carriers, which further enhanced the device's performance. The presented results showed that a G-SS MISFED with a channel length as short as 5 nm can achieve a forward-to-reverse current rectification ratio as high as 5000, representing an enhancement of three orders of magnitude compared to a G-SSD with comparable dimensions. Our approach can readily be adopted for the realization of other types of all-Graphene MIS based structures and devices, such as MIS capacitors or even three-terminal MIS Field Effect Transistors, within a single Graphene monolayer. These results promise a potential for the realization of atomically-thin all-Graphene integrated circuits, which can be highly flexible, highly transparent and very economical.

Methods

Transport calculations for obtaining I-V characteristics curves and transmission pathways plots were all based on the Extended Huckel (EH)[40] method and Non-Equilibrium Green's Function (NEGF) formalism[45] as implemented in Atomistic Tool Kit (ATK) software package[40]. The Semi-Empirical (SE) Tight-Binding (TB) approach was used instead of the computationally expensive Density Functional Theory (DFT) based approach for the large device structures (>500 atoms). This SE EH method treats the effect of the external potential on the entire system (atomic and trench regions) with desirable computational efficiency. Moreover, it has been reported that calculations based on the EH method for such large atomic structures show quantitative agreement with experimental results when compared with DFT-based *ab initio* approaches[40].

Calculation of transport (I-V) characteristics. Prior to transport calculations, the device geometries were optimized and their coordinates were relaxed using the Brenner potential[46] until the forces on individual atoms were minimized to be smaller than 0.05 eV/Å^2. In the nitrogen passivated device structure of Fig. 6(a), nitrogen atoms were substituted for hydrogen atoms.

Each device structure was partitioned as three regions: semi-infinite left electrode (*L*), central scattering region (*C*), and semi-infinite right electrode (*R*). The mesh points in real space calculation were defined as uniformly spaced *k* points of 1 × 10 × 50 for all devices, with 50 sample points along the length (transport direction) and 10 points along the width (induced electric field direction) of the two-terminal structure.

The used tight-binding model was based on the Extended Huckel Method as implemented in ATK-SE package, in which the tight-binding Hamiltonian is parameterized using a two-center approximation, where the matrix elements are described in terms of overlaps between Slater orbitals on each site. The used weighting scheme of the orbital energies of the offsite Hamiltonian was according to Wolfsburg[47]. Further details about the calculation method can be found in Ref. 40.

The electronic transport properties were then calculated using Nonequilibrium Green's Function (NEGF) formalism. The device structure was constructed as the three previously mentioned regions (left-electrode, central-region and right-electrode) and coherent transport of electrons was assumed to occur between left and right electrodes with Fermi levels μ_L and μ_R through the central region. According to Landauer formula[48], the coherent current between the electrodes is given by:

$$I(V) = \frac{2e}{h}\int_{\mu_R}^{\mu_L} T(E,V)[f_0(E-\mu_L) - f_0(E-\mu_R)]dE \quad (1)$$

where $T(E,V)$ is the transmission probability of incident electrons with energy E from left-electrode (L) to right-electrode (R), $f_0(E-\mu_{L(R)})$ is the Fermi-Dirac distribution function of electrons in the L and R electrodes respectively, and $V = \frac{\mu_R - \mu_L}{e}$ is the potential difference between L and R electrodes. The $T(E,V)$ is correlated with $\hat{G}^a(E)$ and $\hat{G}^r(E)$, the Green's function matrices reflected from L and R to the central scattering region respectively, as:

$$T(E,V) = Tr\left[\mathrm{Im}\sum\nolimits_L\left(E-\frac{eV}{2}\right)\hat{G}^r(E)\mathrm{Im}\sum\nolimits_R\left(E+\frac{eV}{2}\right)\hat{G}^a(E)\right] \quad (2)$$

where $\sum_{L(R)}$ are electrodes' self-energies describing the coupling with the central region.

Calculation of transmission pathways. As the Landauer approach only connects the external electrode current $I(V)$ with the summed energy dependent transmission probability $T(E,V)$, we need to express local current components at the atomic level along the chemical bonds to describe the variation of coherent electron transport through the system. Local current components may be investigated by extracting local transmission components. The total transmission coefficient can be split into local bond contributions, T_{ij}, which are represented in ATK by lines along the bond lengths, called transmission pathways. The relationship between the total transmission coefficient and the local bond contributions can be described as:

$$T(E,V) = \sum_{i\in A,\, j\in B} T_{ij}(E,V) \quad (3)$$

where A and B represent pairs of atoms separated by an imaginary surface perpendicular along the bond length. The total transmission coefficient is the sum of the local bond contributions between all pairs of atoms A and B. A negative value of T_{ij} correspond to back scattered electrons along the bond, while a positive value corresponds to transmitted electrons. Further details can be found in Ref. 49.

1. Novoselov, K. S. *et al.* Electric field effect in atomically thin carbon films. *Science* **306**, 666–669 (2004).
2. Geim, A. K. Graphene: Status and prospects. *Science* **324**, 1530–1534 (2009).
3. Avouris, P. Graphene: Electronic and Photonic Properties and Devices. *Nano Lett.* **10**, 4285–4294 (2010).
4. Novoselov, K. S. *et al.* A roadmap for graphene. *Nature* **490**, 192–200 (2012).
5. Lin, Y. M. *et al.* 100-GHz transistors from wafer-scale epitaxial graphene. *Science* **327**, 662 (2010).
6. Wu, Y. *et al.* High-frequency, scaled graphene transistors on diamond-like carbon. *Nature* **472**, 74–78 (2011).
7. Liao, L. *et al.* High-speed graphene transistors with a self-aligned nanowire gate. *Nature* **467**, 305–308 (2010).
8. Wu, Y. *et al.* State-of-the-art graphene high-frequency electronics. *Nano Lett.* **12**, 3062–3067 (2012).
9. Lin, Y. M. *et al.* Wafer-scale graphene integrated circuit. *Science* **332**, 1294–1297 (2011).
10. Wang, H., Nezich, D., Kong, J. & Palacios, T. Graphene frequency multipliers. *IEEE Electron Device Lett.* **30**, 547–549 (2009).
11. Sordan, R., Traversi, F. & Russo, V. Logic gates with a single graphene transistor. *Appl. Phys. Lett.* **94**, 073305 (2009).
12. Britnell, L. *et al.* Field-effect tunneling transistor based on vertical graphene heterostructures. *Science* **335**, 947–950 (2012).
13. Yang, H. *et al.* Graphene barristor, a triode device with a gate-controlled Schottky barrier. *Science* **336**, 1140–1143 (2012).
14. Chen, C. C., Aykol, M., Chang, C. C., Levi, A. F. J. & Cronin, S. B. Graphene-silicon Schottky diodes. *Nano Lett.* **11**, 1863–1867 (2011).
15. Li, X. *et al.* Graphene-on-silicon schottky junction solar cells. *Adv. Mater.* **22**, 2743–2748 (2010).
16. Tongay, S. *et al.* Rectification at graphene-semiconductor interfaces: Zero-gap semiconductor-based diodes. *Phys. Rev. X* **2**, 1–10 (2012).
17. Nourbakhsh, A. *et al.* Modified, semiconducting graphene in contact with a metal: Characterization of the Schottky diode. *Appl. Phys. Lett.* **97**, 163101–163103 (2010).
18. Song, A. *et al.* Unidirectional electron flow in a nanometer-scale semiconductor channel: A self-switching device. *Appl. Phys. Lett.* **83**, 1881–1883 (2003).
19. Balocco, C. *et al.* Microwave detection at 110 GHz by nanowires with broken symmetry. *Nano Lett.* **5**, 1423–1427 (2005).
20. Balocco, C. *et al.* Room-temperature operation of a unipolar nanodiode at terahertz frequencies. *Appl. Phys. Lett.* **98**, 223501 (2011).
21. Chen, Z., Lin, Y. M., Rooks, M. J. & Avouris, P. Graphene nano-ribbon electronics. *Physica E* **40**, 228–232 (2007).
22. Avouris, P., Chen, Z. & Perebeinos, V. Carbon-based electronics. *Nature Nanotech.* **2**, 605–615 (2007).

23. Barone, V., Hod, O. & Scuseria, G. E. Electronic structure and stability of semiconducting graphene nanoribbons. *Nano Lett.* **6**, 2748–2754 (2006).
24. Xie, G. *et al.* Graphene edge lithography. *Nano Lett.* **12**, 4642–4646 (2012).
25. Wang, X. & Dai, H. Etching and narrowing of graphene from the edges. *Nature Chem.* **2**, 661–665 (2010).
26. Tapaszto, L., Dobrik, G., Lambin, P. & Biro, L. P. Tailoring the atomic structure of graphene nanoribbons by scanning tunnelling microscope lithography. *Nat Nanotech.* **3**, 397–401 (2008).
27. Campos, L. C., Manfrinato, V. R., Sanchez-Yamagishi, J. D., Kong, J. & Jarillo-Herrero, P. Anisotropic etching and nanoribbon formation in single-layer graphene. *Nano Lett.* **9**, 2600–2604 (2009).
28. Lemme, M. C. *et al.* Etching of graphene devices with a helium ion beam. *ACS Nano* **3**, 2674–2676 (2009).
29. Bai, J., Duan, X. & Huang, Y. Rational fabrication of graphene nanoribbons using a nanowire etch mask. *Nano Lett.* **9**, 2083–2087 (2009).
30. Xie, L., Jiao, L. & Dai, H. Selective etching of graphene edges by hydrogen plasma. *J. Am. Chem. Soc.* **132**, 14751–14753 (2010).
31. Wang, X. *et al.* Room-Temperature All-Semiconducting Sub-10-nm Graphene Nanoribbon Field-Effect Transistors. *Phys. Rev. Lett.* **100**, 206803 (2008).
32. Cai, J. *et al.* Atomically precise bottom-up fabrication of graphene nanoribbons. *Nature* **466**, 470–473 (2010).
33. Wang, X. *et al.* Graphene nanoribbons with smooth edges behave as quantum wires. *Nature Nanotech.* **6**, 563–567 (2011).
34. Jia, X. *et al.* Controlled formation of sharp zigzag and armchair edges in graphitic nanoribbons. *Science* **323**, 1701–1705 (2009).
35. Du, A. & Smith, S. C. Electronic functionality in graphene-based nanoarchitectures: Discovery and design via first-principles modeling. *J. Phys. Chem. Lett.* **2**, 73–80 (2011).
36. Yan, Q. *et al.* Intrinsic current-voltage characteristics of graphene nanoribbon transistors and effect of edge doping. *Nano Lett.* **7**, 1469–1473 (2007).
37. Behnam, A. *et al.* Transport in nanoribbon interconnects obtained from graphene grown by chemical vapor deposition. *Nano Lett.* **12**, 4424–4430 (2012).
38. Tao, C. *et al.* Spatially resolving edge states of chiral graphene nanoribbons. *Nature Phys.* **7**, 616–620 (2011).
39. Son, Y. W., Cohen, M. L. & Louie, S. G. Energy gaps in graphene nanoribbons. *Phys. Rev. Lett.* **97**, 216803 (2006).
40. Stokbro, K. *et al.* Semiempirical model for nanoscale device simulations. *Phys. Rev. B* **82**, 075420 (2010).
41. Mayorov, A. S. *et al.* Micrometer-scale ballistic transport in encapsulated graphene at room temperature. *Nano Lett.* **11**, 2396–2399 (2011).
42. Saha, K. K., Drndic, M. & Nikolic, B. K. DNA base-specific modulation of microampere transverse edge currents through a metallic graphene nanoribbon with a nanopore. *Nano Lett.* **12**, 50–55 (2012).
43. Wang, X. *et al.* N-doping of graphene through electrothermal reactions with ammonia. *Science* **324**, 768–771 (2009).
44. Yu, S. S. & Zheng, W. T. Effect of N/B doping on the electronic and field emission properties for carbon nanotubes, carbon nanocones, and graphene nanoribbons. *Nanoscale* **2**, 1069–1082 (2010).
45. Brandbyge, M., Mozos, J. L., Ordejón, P., Taylor, J. & Stokbro, K. Density-functional method for nonequilibrium electron transport. *Phys. Rev. B* **65**, 165401 (2002).
46. Brenner, D. W. *et al.* A second-generation reactive empirical bond order (REBO) potential energy expression for hydrocarbons. *J. Phys.: Condens. Matter* **14**, 783–802 (2002).
47. Wolfsberg, M. A. X. & Helmholz, L. The spectra and electronic structure of the tetrahedral ions MnO 4 -, CrO4 -, and ClO4. *J. Chem. Phys.* **20**, 837–843 (1952).
48. Landauer, R. Spatial Variation of Currents and Fields Due to Localized Scatterers in Metallic Conduction. *IBM J. Res. Develop.* **1**, 223–231 (1957).
49. Solomon, G. C., Herrmann, C., Hansen, T., Mujica, V. & Ratner, M. A. Exploring local currents in molecular junctions. *Nature Chem.* **2**, 223–228 (2010).

Acknowledgments

Authors would like to thank the NICTA Optics and Nanoelectronics (ONE) group members for your valuable discussions and feedback. F.A. thanks Dana Hirzalla for helping in the production of figures and thanks Christophe Caloz and Woo Young Choi for their valuable discussions and comments. This work was funded by The National ICT Australia – Victorian Research Laboratory (NICTA-VRL), University of Melbourne, Parkville, VIC 3010, Australia.

Author contributions

E.S. conceived the use of Graphene for SSDs; F.A. conceived the concept of a G-SS MISFED and developed the idea of nitrogen passivation for the device; F.A., A.N. and E.S. contributed to the optimization of device dimensions; F.A. designed the simulations; F.A. and F.M.H. conducted the simulations; all authors analysed the results; F.A. wrote the manuscript; All authors reviewed the manuscript.

Additional information

Competing financial interests: The authors declare no competing financial interests.

How to cite this article: Al-Dirini, F., Hossain, F.M., Nirmalathas, A. & Skafidas, E. All-Graphene Planar Self-Switching MISFEDs, Metal-Insulator-Semiconductor Field-Effect Diodes. *Sci. Rep.* **4**, 3983; DOI:10.1038/srep03983 (2014).